



**HAL**  
open science

## Permeation and trapping of hydrogen in Eurofer97

F. Montupet-Leblond, L. Corso, M. Payet, Rémi Delaporte-Mathurin, E. Bernard, Y. Charles, J. Mougenot, S. Vartanian, E.A. A Hodille, C. Grisolia

### ► To cite this version:

F. Montupet-Leblond, L. Corso, M. Payet, Rémi Delaporte-Mathurin, E. Bernard, et al.. Permeation and trapping of hydrogen in Eurofer97. Nuclear Materials and Energy, 2021, 29, pp.101062. 10.1016/j.nme.2021.101062 . hal-03355595

**HAL Id: hal-03355595**

**<https://hal.science/hal-03355595v1>**

Submitted on 27 Sep 2021

**HAL** is a multi-disciplinary open access archive for the deposit and dissemination of scientific research documents, whether they are published or not. The documents may come from teaching and research institutions in France or abroad, or from public or private research centers.

L'archive ouverte pluridisciplinaire **HAL**, est destinée au dépôt et à la diffusion de documents scientifiques de niveau recherche, publiés ou non, émanant des établissements d'enseignement et de recherche français ou étrangers, des laboratoires publics ou privés.

# Permeation and trapping of hydrogen in Eurofer97

F. Montupet-Leblond<sup>a,\*</sup>, L. Corso<sup>a</sup>, M. Payet<sup>a</sup>, R. Delaporte-Mathurin<sup>a,b</sup>, E. Bernard<sup>a</sup>, Y. Charles<sup>b</sup>, J. Mougenot<sup>b</sup>, S. Vartanian<sup>a</sup>, E. A. Hodille<sup>a</sup>, C. Grisolia<sup>a</sup>

<sup>a</sup>*Institut de Recherche sur la Fusion par Confinement Magnétique, CEA Cadarache, 13115 St Paul lez Durance, France*

<sup>b</sup>*Université Sorbonne Paris Nord, Laboratoire des Sciences des Procédés et des Matériaux, LSPM, CNRS, UPR 3407, F-93430, Villetaneuse, France*

---

## Abstract

Diffusion and trapping of hydrogen isotopes in fusion materials need to be fully described in order to evaluate permeation and retention in fusion reactors walls and breeding blankets. Hydrogen gas permeation experiments have been conducted on Eurofer97 with pressures ranging from  $10^1$  to  $10^5$  Pa and temperatures between 473 K and 673 K, resulting in solubility  $K(T)$  ( $\text{mol}\cdot\text{m}^{-3}\cdot\text{Pa}^{-1/2}$ ) =  $1.76 \cdot 10^{-1} \exp(-0.27 \text{ (eV)}/k_B T)$ , diffusivity  $D(T)$  ( $\text{m}^2\cdot\text{s}^{-1}$ ) =  $2.52 \cdot 10^{-7} \exp(-0.16 \text{ (eV)}/k_B T)$  and permeability  $\Phi(T)$  ( $\text{mol}\cdot\text{m}^{-1}\cdot\text{Pa}^{-1/2}\cdot\text{s}^{-1}$ ) =  $4.43 \cdot 10^{-8} \exp(-0.43 \text{ (eV)}/k_B T)$ . Trapping parameters have been investigated using thermal desorption spectrometry of deuterium-loaded samples coupled with parametric optimization, leading to detrapping energies  $E_{dt,1} = 0.51$  eV,  $E_{dt,2} = 1.27$  eV,  $E_{dt,3} = 1.65$  eV and densities  $N_{t,1} = 6.01 \cdot 10^{25} \text{ m}^{-3}$ ,  $N_{t,2} = 6.44 \cdot 10^{22} \text{ m}^{-3}$ ,  $N_{t,3} = 3.88 \cdot 10^{23} \text{ m}^{-3}$ . This parametric optimization is performed using a kinetic surface model: the contribution of this model is compared to the results given by solubility and recombination rate models.

**Keywords:** Permeation, Trapping, Eurofer97, Hydrogen, Thermal Desorption Spectrometry, MHIMS, surfaces

---

## 1. Introduction

Tritium permeation and inventory in the walls of fusion reactors need to be assessed to comply with safety and environmental regulations. The foreseen design for DEMO plasma facing components and breeding blankets includes Eurofer as a structural material [1, 2], which calls for investigation of the transport and trapping characteristics of this low-activation steel.

To that end, hydrogen permeation experiments were conducted on Eurofer97 samples in order to measure diffusivity, permeability and trapping parameters and evaluate solubility of hydrogen in this material. These results show that hydrogen transport parameters are affected by trapping in the 400 K - 700 K range. As permeation measurements only give an integrated vision of trapping (in the occurrence of multiple trapping sites, permeation is not able to discriminate between trapping sites), thermal desorption spectrometry (TDS) experiments were performed on deuterium-loaded Eurofer97 in order to give a more detailed understanding of trapping in this material. The experimental results were analyzed using a macroscopic diffusion/reaction model implemented in the MHIMS code [3] including a kinetic surface model [4]. The detrapping energies and densities of trapping sites, as well as parameters that render the kinetics of hydrogen on the surface, are obtained

from these simulations. These results altogether are shown to be in agreement, giving a complete set of parameters describing hydrogen permeation and trapping in Eurofer97. The improvement brought to the model by the kinetic surface model is shown by comparing the results with a recombination rate model.

## 2. Gas permeation

In a gas permeation experiment, the sample (typically disk-shaped) is exposed to a stepwise increase of gas pressure on one side while the other side is under vacuum. This unbalance drives the particles to permeate through the sample, creating a pressure rise on the downstream side. This downstream pressure rise can be analyzed using the timelag method (see section 2.4) to yield permeation parameters such as diffusivity and permeability (see section 2.1). The work presented here aims at describing a new hydrogen permeation setup, which was used to measure the transport parameters of hydrogen in Eurofer97.

### 2.1. Theoretical aspects

Hydrogen transport parameters such as diffusivity  $D$  and permeability  $\Phi$  can be evaluated based on the pressure rise in the case of diffusion-limited regime (see section 2.4). Hydrogen solubility  $K$ , also called Sieverts' constant, is then calculated as the ratio of these quantities using the

---

\*Corresponding author

Email address: [floriane.leblond@cea.fr](mailto:floriane.leblond@cea.fr)  
(F. Montupet-Leblond)

defining relation

$$\Phi(T) = D(T) \cdot K(T) \quad (1)$$

where  $T$  is the sample temperature, given in K.

Hydrogen isotopes permeation is affected by trapping: once in the bulk, dissolved atoms are likely to remain trapped at specific locations, such as dislocations or vacancies, which slows down the migration of hydrogen. Therefore, permeation experiments do not yield  $D$  and  $K$ , which correspond respectively to interstitial diffusion and interstitial dissolution, but effective diffusivity  $D_{\text{eff}}$  and effective solubility  $K_{\text{eff}}$ , defined as follows [5]:

$$D(T) = D_0 \exp\left(-\frac{E_D}{k_B T}\right) \quad (2)$$

$$K(T) = K_0 \exp\left(-\frac{E_K}{k_B T}\right) \quad (3)$$

$$D_{\text{eff}}(T) = D(T) \cdot \left(1 + \frac{N_t}{N_l} \exp\left(\frac{E_b}{k_B T}\right)\right)^{-1} \quad (4)$$

$$K_{\text{eff}}(T) = K(T) \cdot \left(1 + \frac{N_t}{N_l} \exp\left(\frac{E_b}{k_B T}\right)\right) \quad (5)$$

$D_0$  and  $K_0$  are the pre-exponential diffusivity and solubility factors (resp.  $\text{m}^2 \cdot \text{s}^{-1}$  and  $\text{mol} \cdot \text{m}^{-3} \cdot \text{Pa}^{-1/2}$ );  $E_D$  (eV) is the energy barrier for the diffusion between interstitial sites,  $E_K$  (eV) is the solution energy of H in interstitial sites (defectless material) and  $E_b$  (eV) is the binding energy of hydrogen to traps. Detrapping energy is usually taken as the sum of binding energy  $E_b$  and diffusive energy  $E_D$ , as shown in figure 1.  $N_t$  and  $N_l$  ( $\text{m}^{-3}$ ) are the trap sites and lattice diffusion sites concentrations. Equations (4) and (5) bear the assumption that a single trapping site affects diffusivity and solubility of hydrogen in the considered range of temperature. If other trapping sites (non-dominant) are present, they do not affect  $D_{\text{eff}}$ . Another measurement technique called thermal desorption spectrometry (TDS) detailed in part 3 can help us determine the properties of those secondary traps. In particular, if high energy traps are present, they would be filled during the first exposure to H and become transparent for permeation in the following measurement cycles.

Combining equations (1) and (2)-(3) gives the defining relation for permeability:

$$\Phi(T) = \Phi_0 \exp\left(-\frac{E_\Phi}{k_B T}\right) \quad (6)$$

where  $\Phi_0 = D_0 \cdot K_0$  ( $\text{mol} \cdot \text{m}^{-1} \cdot \text{Pa}^{-1/2} \cdot \text{s}^{-1}$ )

$$E_\Phi = E_D + E_K \text{ (eV)}$$

Equations (2)-(5) show in particular that the influence of traps is stronger at lower temperatures. Schematically,  $D_{\text{eff}}$  and  $K_{\text{eff}}$  are driven by trapping effects at lower

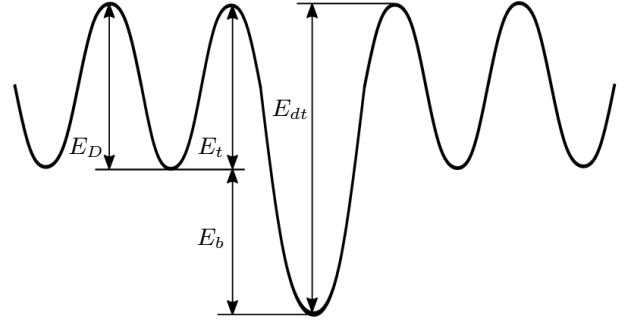


Figure 1: Energy diagram presenting diffusion energy  $E_D$ , trapping energy  $E_t$ , binding energy  $E_b$  and detrapping energy  $E_{dt}$ . This diagram illustrates the assumption that  $E_D = E_t$  and explicits the relation between trapping, detrapping and diffusion :  $E_{dt} = E_D + E_b$

temperatures, while lattice properties have the upper hand at higher temperatures.

During the permeation analysis,  $D_{\text{eff}}$  and  $\Phi$  are measured at several temperatures, after which  $D_{\text{eff}}(T)$  is fitted numerically using equation (4) with  $D_0$ ,  $E_D$ ,  $N_t$  and  $E_b$  as free parameters. The interstitial sites density is  $N_l = 5.15 \cdot 10^{29} \text{ sites} \cdot \text{m}^{-3}$ , assuming that H sits in tetrahedral interstitial positions of a bcc structure in Eurofer97 [4]. Once  $\Phi$  and  $D_{\text{eff}}$  are known,  $K_{\text{eff}}$  is calculated using equation (1).

## 2.2. State of the art

Gas permeation experiments performed on Eurofer97 between 423 K and 723 K yielding diffusivity, solubility and permeability of hydrogen isotopes have been presented in [5], [6] and [7], respectively with hydrogen and deuterium. Through the evolution of effective diffusivity versus temperature, the results show that trapping has an impact on the transport parameters in the 400 K - 700 K range. Effective diffusivity is consequently fitted using equation (4), where  $E_b$  is seen as the mean interaction energy between hydrogen isotopes and trapping sites. Based on the value of this energy, trapping in Eurofer97 is assumed to be caused by high angle grain boundaries [5] or interfaces between martensitic laths and carbide precipitates or dislocations [6, 8].

## 2.3. Experimental setup

The diagram of the Hypertomate setup (HYdrogen PERmeation in TOKamak-relevant MATERials) is given in figure 2. In this setup, two high-vacuum chambers are separated by a thin sample. During a run of the experiment, hydrogen is introduced stepwise in one of the chambers (called the upstream part), creating a flux through the sample. This permeation flux induces a pressure rise on the downstream part. The dynamics of

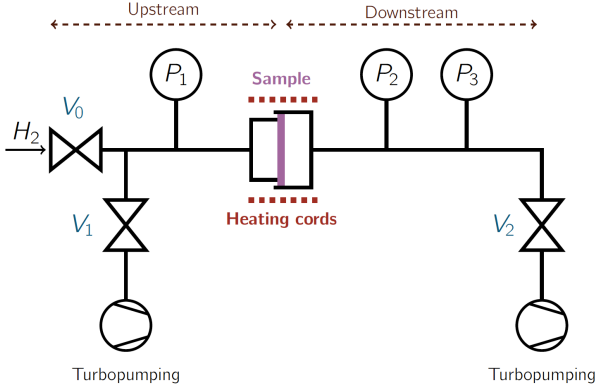


Figure 2: Diagram presenting the Hypertomate hydrogen permeation experiment

this pressure rise contain information about the sample material, such as diffusivity and permeability.

On both sides, the pressure is recorded using MKS<sup>®</sup> Baratron gauges (1000 Torr full gauge on the upstream side, 0.1 Torr full scale downstream), making the measurement independent of the gas. Hydrogen is introduced stepwise in the upstream part, where the pressure is controlled by a MKS<sup>®</sup> Baratron pressure gauge ( $P_1$ , 1000 Torr full scale). Volume has been minimized in order for small permeation fluxes to translate into relevant pressure signals.

Upstream and downstream pressure measurements are sampled on a multiplexer in order to measure the timelag with the method presented in figure 3. As the permeation flux is measured through the pressure rise only, it is not possible to discriminate between hydrogen and other species in the permeation flux. Thorough leak detections, careful preliminary conditioning of the vacuum chambers and background recordings are performed at each step and the background noise is systematically checked to be negligible compared to the permeation flux.

#### 2.4. Data analysis

The first step of the analysis is the characterization of the permeation regime, which can be either diffusion-limited or surface-limited [9]. The distinction is made using the exponential relationship between the steady-state permeating flux  $J$  ( $\text{Pa}\cdot\text{m}^{-3}\cdot\text{s}^{-1}$ ) and the upstream pressure  $p_{\text{up}}$  (Pa):

- If  $J \propto p_{\text{up}}^{1/2}$ , permeation is diffusion-limited. In this case, the timelag method (see 2.4) can be used to calculate  $D_{\text{eff}}$ , and  $\Phi$  is linked to  $p_{\text{up}}$  by

$$J = \frac{\Phi}{e} p_{\text{up}}^{1/2} \quad (7)$$

where  $e$  (m) is the thickness of the material.

- If  $J \propto p_{\text{up}}$ , permeation is surface-limited and

$$J = \frac{1}{2} \sigma k_1 p_{\text{up}} \quad (8)$$

where  $\sigma k_1$  ( $\text{m}^{-3}\cdot\text{s}^{-1}$ ) is the adsorption rate constant on the upstream side of the sample. In that case, the pressure rise is influenced by the surface effects taking place on the upstream side and the bulk effects are negligible; therefore, the bulk parameters  $D_{\text{eff}}$  and  $\Phi$  cannot be extracted from the pressure rise.

This characterization step has to be performed at each temperature. After the permeation regime has been proven to be diffusion-limited,  $\Phi$  is directly calculated using equation (7). Effective diffusivity is evaluated using the timelag method with

$$\tau_l = \frac{e^2}{6D_{\text{eff}}} \quad (9)$$

This well-established method first introduced in [10] uses the asymptote of the steady-state pressure, shown in red in figure 3. The timelag is defined as the time interval between the upstream pressure introduction and the intersection of this asymptote with the time axis.

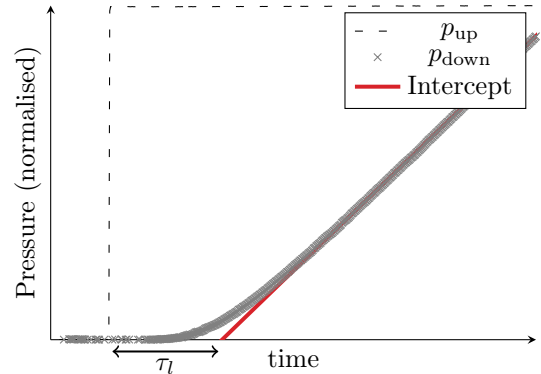


Figure 3: Timelag method illustration

In order for the timelag measurement to be valid, the upstream pressure rise has to be as close as possible to a step function.

#### 2.5. Results

Measurements following the procedure described earlier have been performed on two disk-shaped samples of Eurofer97 with diameter 20 mm and thicknesses 974 and 945  $\mu\text{m}$ , cut from the same rod, with temperatures between 473 and 573 K and loading pressures ranging from  $10^2$  to  $10^5$  Pa. The samples were analyzed using X-ray fluorescence and their composition is given in table 1. Prior to the measurements, the samples were mechanically polished to mirror finish and cleaned in ethanol. No annealing was performed in order to measure the properties of coarse Eurofer97.

Before each measurement, the pressure is checked to be around  $1 \cdot 10^{-4}$  Pa on each side on the sample. Valve 2 is then closed and the subsequent background pressure rise is recorded in order to be subtracted from the permeation signal. In most configurations, this background signal is well under 1% of the permeation-induced pressure rise. This method results in error bars under 10% for both  $D_{\text{eff}}$  and  $\Phi$  at each temperature, showing good reproducibility for this experimental setup.

Element	Z	Concentration (mass ratio)
Fe	26	82.88 %
Cr	24	8.84 %
Cu	29	2.46 %
W	74	1.11 %
Na	11	0.59 %
Mn	25	0.53 %
V	23	0.19 %
Se	34	547 ppm
Co	27	213 ppm
K	19	201 ppm
Zn	30	193 ppm

Table 1: Eurofer97 detailed composition

Diffusion-limited behaviour is validated by plotting  $\log(J)$  versus  $\log(p_{\text{up}})$  and checking that the slope is close to 0.5. An example of this validation, performed at 300°C, is given in figure 4.

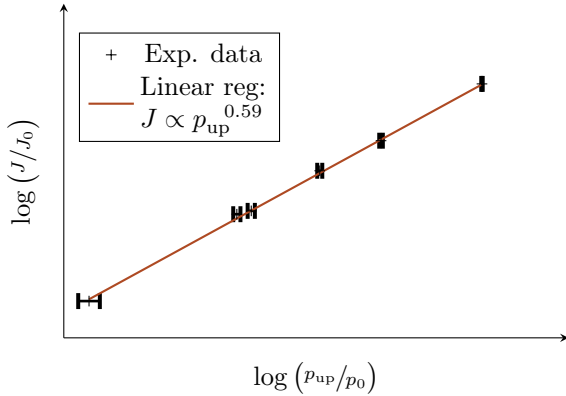
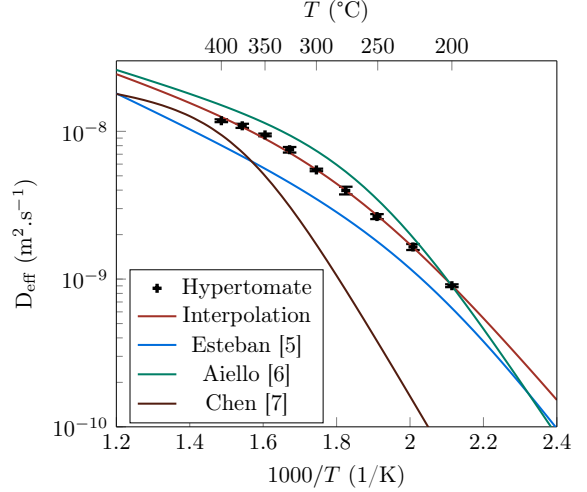


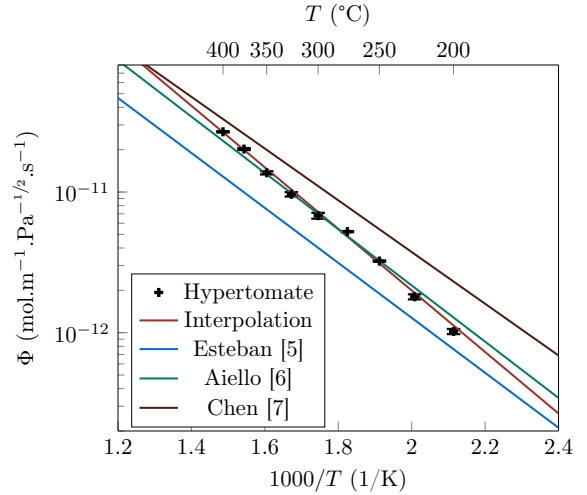
Figure 4: Permeation regime characterisation

Once the permeation is ruled to be diffusion-limited, the timelag method and equation (7) are used to determine respectively  $D_{\text{eff}}$  and  $\Phi$ . The results are shown in figures 5a (effective diffusivity  $D_{\text{eff}}$ ), 5b (permeability  $\Phi$ ) and 5c (effective solubility  $K_{\text{eff}}$ ). The plots also display previously obtained values for Eurofer97 taken from [5] and [6], showing that Hypertomate results are in good agreement with literature. In particular, [6] gives permeation parameters for deuterium in Eurofer97. For the comparison to be relevant, diffusivity and permeability are corrected using a mass ratio factor given by [11]:

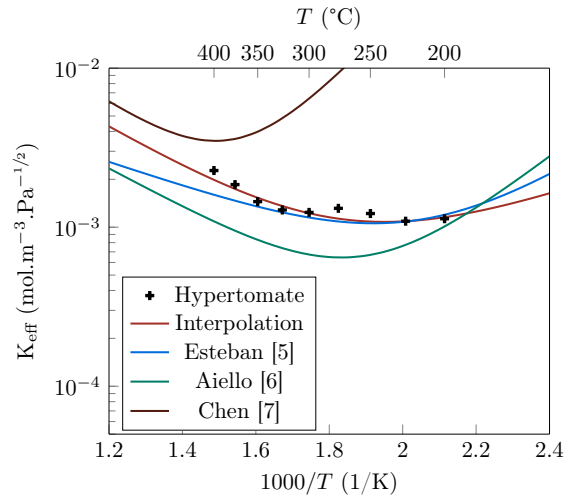
$$\frac{D_{\text{H}}}{D_{\text{D}}} = \sqrt{\frac{m_{\text{D}}}{m_{\text{H}}}} = \sqrt{2} \quad (10)$$



(a) Hydrogen effective diffusivity in Eurofer97



(b) Hydrogen permeability in Eurofer97



(c) Hydrogen effective solubility in Eurofer97

Figure 5: Eurofer97 hydrogen permeation parameters. Fitting experimental results using equations (4) and (6) yield respectively  $D_{\text{eff}}$  and  $\Phi$  while  $K_{\text{eff}}$  is calculated as their ratio  $\Phi/D_{\text{eff}}$  following (1).

The corresponding quantities describing hydrogen transport in Eurofer97 ( $D_{\text{eff}}(T)$ ,  $K_{\text{eff}}(T)$  and  $\Phi(T)$ ), measured using Hypertomate, compare well with the previously published values [5, 6]. However, the transport parameters given in [7] differ from the other ones, especially at low temperatures. This issue was pointed out in [7] and calls for further work.

The corresponding Arrhenius parameters, obtained by weighted least-squares fitting, are given in table 2.

### 3. Thermal desorption spectrometry

Thermal Desorption Spectrometry (TDS) consists in heating up a previously loaded sample following a given temperature ramp-up. Desorption from the trapping sites ensues, measured by a mass spectrometer. The spectrum typically shows peaks which can be attributed to trapping sites. The work presented here includes a TDS spectrum for Eurofer97 loaded with deuterium by gas exposure, as well as the identification of the trapping and surface parameters through parametric optimization performed with the code MHIMS.

#### 3.1. State of the art

Previously performed thermal desorption spectrometry experiments on hydrogen- or deuterium-loaded Eurofer97 show a main desorption peak around 425 K - 500 K [7, 12, 13, 14] for heating rates varying from 6 to 20 K/s and several loading techniques (plasma implantation, gas loading and electrochemical loading). These spectra also show a similar behavior in the low-temperature range, with a desorption rate close to zero until around 400 K. Although the loading conditions and heating rates differ in [15], [16] and [17], the corresponding Eurofer97 TDS spectra present up to three desorption bands. Single peak Eurofer97 TDS spectra are witnessed in the case of plasma loading ([14]), electrochemical loading ([12, 13, 18]) and short (1h) gas loading [7]: if these surnumerary traps are located deep enough in the bulk, short gas loading or plasma implantation do not fill them right away, but the waiting time between loading and TDS lets the atoms migrate in the material and fill these two traps.

#### 3.2. Sample preparation and measurement

In order to supplement the analysis with a more thorough set of trapping parameters, thermal desorption spectrometry (TDS) is performed on Eurofer97 samples using the device described in [19].

Similarly to permeation, the sample is not annealed in order to be representative of coarse Eurofer97. Loading is performed by heating up the sample at 400°C in a deuterium gas atmosphere of  $9 \cdot 10^4$  Pa for 6 hours. The

conditions of this gentle loading are similar to those of permeation, which allows us to compare the two experiments. At the end of loading, the vial containing the sample and the deuterium atmosphere is quenched in room-temperature water.

The TDS experiment is conducted in a high vacuum chamber equipped with a Bayard-Alpert pressure gauge and a mass spectrometer. After each measurement, the mass spectrometer is calibrated by injecting  $D_2$  in the chamber and recording the corresponding pressure. Prior to heating up the sample, the residual pressure in the chamber is  $p_{bg} \sim 1 \cdot 10^{-6}$  Pa dominated by residual  $H_2O$ . During the experiment, the loaded sample is heated following a ramp-up of 1 K/s up to 873 K. The maximum temperature is capped in order to avoid a phase change in Eurofer97 [20]. The sample temperature is controlled and recorded by a thermocouple inserted in the sample, which guarantees a constant heating rate and an accurate measurement of the sample temperature. At the end of the TDS measurement, the sample is let to cool down in the vacuum chamber before performing the measurement a second time. This step is necessary to ensure that deuterium has fully desorbed in the temperature range covered by the experiment and also serves as a background measurement, proving that the sample heating does not interfere with the spectrometer measurements.

#### 3.3. Experimental results

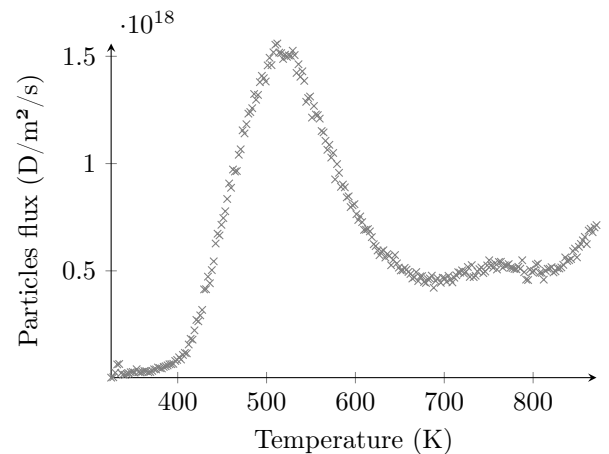


Figure 6: Thermal desorption spectrometry spectrum of deuterium in Eurofer97. The sample was loaded under deuterium atmosphere of  $9 \cdot 10^4$  Pa at 673 K for 6 hours. TDS was then performed with a 1 K/s temperature ramp-up.

The resulting spectrum is presented in figure 6. This desorption spectrum shows a prominent peak centered on 510 K. A second peak is appearing at the end of temperature range, interrupted. A temperature ramp-up performed on an empty sample showed that this high temperature behaviour is not an artifact of the measurement technique. The shape of this TDS can be interpreted as a first trap with relatively low detrapping

	$D_0$ ( $\text{m}^2 \cdot \text{s}^{-1}$ )	$E_D$ (eV)	$\Phi_0$ ( $\text{mol} \cdot \text{m}^{-1} \cdot \text{Pa}^{-1/2} \cdot \text{s}^{-1}$ )	$E_\Phi$ (eV)	$K_0$ ( $\text{mol} \cdot \text{m}^{-3} \cdot \text{Pa}^{-1/2}$ )	$E_K$ (eV)	$N_t$ ( $\text{m}^{-3}$ )	$E_b$ (eV)
Hypertomate	$2.52 \cdot 10^{-7}$	0.16	$4.43 \cdot 10^{-8}$	0.43	$1.76 \cdot 10^{-1}$	0.27	$6.08 \cdot 10^{25}$	0.42
Esteban [5]	$4.57 \cdot 10^{-7}$	0.23	$1.03 \cdot 10^{-8}$	0.39	$2.25 \cdot 10^{-2}$	0.16	$1.30 \cdot 10^{25}$	0.45
Aiello [6]	$1.50 \cdot 10^{-7}$	0.15	$1.53 \cdot 10^{-8}$	0.40	$1.02 \cdot 10^{-3}$	0.25	$1.04 \cdot 10^{24}$	0.60
Chen [7]	$3.15 \cdot 10^{-8}$	0.06	$1.26 \cdot 10^{-8}$	0.36	$4.00 \cdot 10^{-1}$	0.30	$4.50 \cdot 10^{23}$	0.78

Table 2: Arrhenius permeation parameters for hydrogen isotopes in Eurofer97

energy and high density, and a second trap with a higher detrapping energy and a seemingly lower density. The final desorption rate is not zero, meaning that some deuterium remains in the sample at the end of the experiment and that the trap in the 850 K region was not fully emptied.

### 3.4. Modeling

To estimate the kinetic trapping and detrapping parameters, a macroscopic rate equation model coupling hydrogen diffusion between interstitial sites and trapping/detrapping based on the McNabb and Forster equations [21] was used. Several codes are available to describe retention and desorption from plasma facing materials and to simulate TDS experiments (MHIMS [3], TESSIM [22], TMAP [23], FESTIM [24], HIDE [25]). These codes share a similar model for diffusion and trapping of hydrogen in a given metal. The difference lies in the boundary condition used to describe the interaction of hydrogen with the surface. The usual approach is to use a recombination coefficient [26]. In particular, TMAP relies on the *ratedep* boundary condition [23], which corresponds to the recombination rate model presented in subsection 4.2. However, the use of this recombination coefficient is based on the assumption that bulk to surface processes are fast. By using a code that implements more fundamental aspects of the surface processes such as MHIMS [3] or TESSIM [22], the simulations go beyond this assumption.

The simulation is done in four steps:

1. Gas loading: constant temperature of 673 K and deuterium loading pressure of  $9 \cdot 10^4$  Pa.
2. Resting phase: temperature is lowered to 300 K. Consequently, deuterium pressure decreases to  $4 \cdot 10^4$  Pa. This step represents the quenching performed during the experimental preparation of the sample.
3. Pumping down: temperature remains at 300 K and deuterium pressure drops to 0 Pa, corresponding to the insertion of the sample in the vacuum enclosure.
4. TDS phase: deuterium pressure is 0 Pa on both sides, corresponding to the vacuum atmosphere of the device. Temperature is increased by 1 K/s, starting at 300 K.

The output of the simulation steps is the desorption rate as a function of temperature. This numeric result is

compared to the experimental spectrum, from which a new set of parameters is inferred.

The evolution of mobile ( $C_m$ ) and trapped ( $C_{t,i}$ ) particles in the bulk is described by equations (11)-(12):

$$\frac{\partial C_{t,i}}{\partial t} = -\nu_0 C_{t,i} \exp^{-\frac{E_{dt,i}}{k_B T}} + \nu_0 \exp^{-\frac{E_D}{k_B T}} \frac{N_{t,i}}{N_i} C_m \left(1 - \frac{C_{t,i}}{N_{t,i}}\right) \quad (11)$$

$$\frac{\partial C_m}{\partial t} = D(T) \frac{\partial^2 C_m}{\partial x^2} - \sum \frac{\partial C_{t,i}}{\partial t} \quad (12)$$

where  $\nu_0$  ( $\text{s}^{-1}$ ) is the pre-exponential frequency for trapping,  $E_{dt,i}$  (eV) is the detrapping energy for trap  $i$  and is  $N_{t,i}$  ( $\text{m}^{-3}$ ) the associated density.

As the sample is exposed on both sides during implantation, and as the desorption is equivalent on both sides of the sample, half of the sample is simulated and a Neumann boundary condition following  $\frac{\partial C_m}{\partial t} = 0$  renders the symmetry.

To simulate gas exposure, several boundary conditions are available:

- Detailed surface model decomposing the surface processes as proposed in [27] and detailed in subsection 3.5;
- Sieverts' law  $C_{m_0} = K \sqrt{p_{\text{load}}}$  where  $C_{m_0}$  is the mobile concentration at the first layer of the bulk in  $\text{mol} \cdot \text{m}^{-3}$ , giving a Dirichlet boundary condition that corresponds to equilibrium in the surface model;
- Recombination model, imposing a recombination flux  $J_r = K_r C_{m_0}^2$  and, as a counterpart, a dissociation flux  $J_d = K_d P_{\text{up}}$ . The recombination rate  $K_r$  can be linked to the surface rate constants as shown in [4]:

$$K_r(T) = \frac{\nu_{bs}^2(T) \nu_{des}(T)}{\nu_{sb}^2(T)} \quad (13)$$

where  $\nu_{bs}$  is the resurfacing rate,  $\nu_d$  is the desorption rate and  $\nu_{sb}$  is the absorption rate, which are detailed in 3.5. These two rates follow Arrhenius laws:

$$K_r(T) = K_{r_0} \exp\left(\frac{-E_{K_r}}{k_B T}\right)$$

$$K_d(T) = K_{d_0} \exp\left(\frac{-E_{K_d}}{k_B T}\right)$$

with  $K_{r_0}$  in  $\text{m}^4 \cdot \text{s}^{-1}$ ,  $K_{d_0}$  in  $\text{mol}^2 \cdot \text{m}^{-2} \cdot \text{Pa}^{-1} \cdot \text{s}^{-1}$  and recombination/dissociation energies in eV. Assuming that the surface processes are in steady-state, recombination and dissociation rates are linked by solubility:

$$K(T) = \sqrt{\frac{K_d(T)}{K_r(T)}} \quad (14)$$

### 3.5. Dynamic surface model

This model takes into account all the fluxes taking place on the surface from  $\text{H}_2$  dissociation to H absorption in the bulk [4, 27]. The equations initially given in [4] are completed with the gas loading flux first presented in [27], giving equations (15) - (16):

$$\frac{\partial C_s}{\partial t} = \phi_{\text{gas}} - \phi_{\text{des}} - \phi_{\text{s} \rightarrow \text{b}} + \phi_{\text{b} \rightarrow \text{s}} \quad (15)$$

$$\lambda \left( \frac{\partial C_m}{\partial t} \right)_{x=0} = \phi_{\text{s} \rightarrow \text{b}} - \phi_{\text{b} \rightarrow \text{s}} - \phi_{\text{diff}} \quad (16)$$

where  $C_s$  is the surface concentration and  $\lambda$  (m) is the distance between two adjacent interstitial sites, and

- $\phi_{\text{gas}} = 2\Gamma \cdot s \cdot p_{\text{load}}(1 - \theta)^2$  is the part of the incident flux of gas molecules that dissociates and sticks on the surface.  $\Gamma = 4.67 \cdot 10^{24} / \sqrt{MT}$  ( $\text{Pa}^{-1} \cdot \text{m}^{-2} \cdot \text{s}^{-1}$ ) is a coefficient depending on molecular mass and temperature taken from kinetic gas theory,  $s = s_0 \exp^{-2E_{\text{diss}}/kT}$  is the initial sticking probability of the impinging atoms with  $s_0$  (dimensionless) the exponential pre-factor for this probability and  $E_{\text{diss}}$  (eV) half the dissociation energy barrier for the  $\text{D}_2$  molecules on the surface.  $p_{\text{load}}$  (Pa) is the loading pressure and  $\theta = C_s/n_s$  is the surface coverage, with  $n_s$  ( $\text{m}^{-2}$ ) the number of sites on the surface.
- $\phi_{\text{des}} = 2\nu_d(T)C_s^2$  is the desorption flux of atoms leaving the surface as molecules. The desorption rate is  $\nu_d(T) = \nu_{0,d}\lambda_d^2 e^{-\frac{2E_{\text{des}}}{kT}}$  where  $\nu_{0,d}$  ( $\text{s}^{-1}$ ) is the desorption frequency,  $\lambda_d = \frac{1}{\sqrt{n_s}}$  (m) is the jumping distance between two surface adsorption sites and  $E_{\text{des}}$  (eV) is half the energy barrier corresponding to the desorption of a  $\text{D}_2$  molecule.
- $\phi_{\text{s} \rightarrow \text{b}} = \nu_{\text{sb}}(T)C_s$  models the absorption of a HI atom from the surface to the bulk, assuming that the mobile concentration is low i.e.  $C_m \ll N_l$ . The absorption rate is  $\nu_{\text{sb}}(T) = \nu_{0,\text{sb}} e^{-E_A/kT}$  where  $\nu_{0,\text{sb}}$  ( $\text{s}^{-1}$ ) represents the absorption frequency and  $E_A$  (eV) is the absorption energy.
- $\phi_{\text{b} \rightarrow \text{s}} = \nu_{\text{bs}}C_{m0}(1 - \theta)$  represents the release of a HI atom from the bulk to the surface. The resurfacing rate is  $\nu_{\text{bs}}(T) = \nu_{0,\text{bs}}\lambda_{\text{bs}} e^{-E_R/kT}$  where  $\nu_{0,\text{bs}}$  represents the frequency associated to the process ( $\text{s}^{-1}$ ),  $E_R$  (eV) is the resurfacing energy and

$\lambda_{\text{bs}} = n_s/N_l$  (m) the jumping distance between the first lattice site encountered by the HI and the initial adsorption site.

- $\phi_{\text{diff}} = -D(T)(\partial C_m/\partial x)_{x=0}$  models the diffusion of the absorbed atoms from the first lattice site in the bulk to deeper lattice sites.

### 3.6. Parametric optimization

In the optimization, all three boundary condition options have been explored in order to show the influence of surface processes on the desorption of deuterium from Eurofer97. In the fit of the experimental TDS signal, the following parameters are left free, with energies taken as constants:

- Detrapping energies  $E_{\text{dt},i}$
- Trapping densities  $N_{t,i}$
- Resurfacing energy  $E_R$
- Absorption energy  $E_A$
- Desorption energy  $E_{\text{des}}$

The last three parameters only concern the kinetic surface model. For this optimization to remain consistent with the permeation results, the free parameters  $E_R$ ,  $E_A$  and  $E_{\text{des}}$  are constrained by equation (18), which is yielded by steady-state in (15)-(16) as shown in [27]:

$$K_0 = \frac{1}{\lambda_{\text{abs}}} \sqrt{\frac{\Gamma s_0}{\nu_0 \lambda_{\text{des}}^2}} \quad (17)$$

$$E_K = E_A - E_{\text{des}} - E_R \quad (18)$$

The rest of the parameters are fixed and given in table 3. In particular,  $s_0$  is calculated using equation (17) in order to fit the solubility measured by Hypertomate and given in table 2.

#### 3.6.1. Detailed surface model

In this part, the experimental TDS is fitted using the kinetic surface model described in 3.5. Results are shown in figure 7.

In this optimization, diffusivity and solubility are taken from Hypertomate. The first guess on detrapping energies and traps densities is based on the previously obtained trapping parameters, namely  $E_b$  and  $N_t$ .

The first round of optimization is performed using two traps. This configuration gives an acceptable fit regarding the peaks width and centering along the temperature axis, showing a good prediction of trapping energies. However, this fit does not predict the desorption taking place around 750 K, as shown by the discrepancy between the green plot and the experimental points on figure 7. In order to bridge this gap, a third trapping site needs to be added to improve



Name	Symbol	Value	Unit	Reference
Diffusivity pre-exponential factor	$D_0$	$2.52 \cdot 10^{-7}$	$\text{m}^2 \cdot \text{s}^{-1}$	this work
Diffusion energy	$E_D$	0.16	eV	this work
Solubility pre-exponential factor	$K_0$	$1.76 \cdot 10^{-1}$	$\text{mol} \cdot \text{m}^{-3} \cdot \text{Pa}^{-1/2}$	this work
Solubility energy	$E_K$	0.27	eV	this work
Sticking probability pre-exponential factor	$s_0$	$1.61 \cdot 10^{-4}$	dimensionless	[27]
Dissociation energy	$E_{\text{diss}}$	0	eV	[28]
bcc iron lattice constant	$a$	2.856	Å	[29]
Eurofer97 density	$\rho_{\text{Eu}}$	$2/a^3 = 8.59 \cdot 10^{28}$	$\text{m}^{-3}$	[4]
Number of adsorption sites on the surface	$n_s$	$\rho_{\text{Eu}}^{2/3} = 1.95 \cdot 10^{19}$	$\text{m}^{-2}$	[4]
Number of interstitial sites in the bulk	$N_l$	$6 \cdot \rho_{\text{Eu}} = 5.15 \cdot 10^{29}$	$\text{m}^{-3}$	[4]
Distance between two adjacent interstitial sites	$\lambda$	$a/2\sqrt{2} = 101 \cdot 10^{-12}$	m	
	$\nu_{0,d}$			
Pre-exponential desorption, absorption, resurfacing and detrapping frequencies	$\nu_{0, \text{sb}}$	$1 \cdot 10^{13}$	$\text{s}^{-1}$	[4]
	$\nu_{0, \text{bs}}$			
	$\nu_0$			

Table 3: Simulation parameters used in the MHIMS code to replicate Eurofer97 TDS

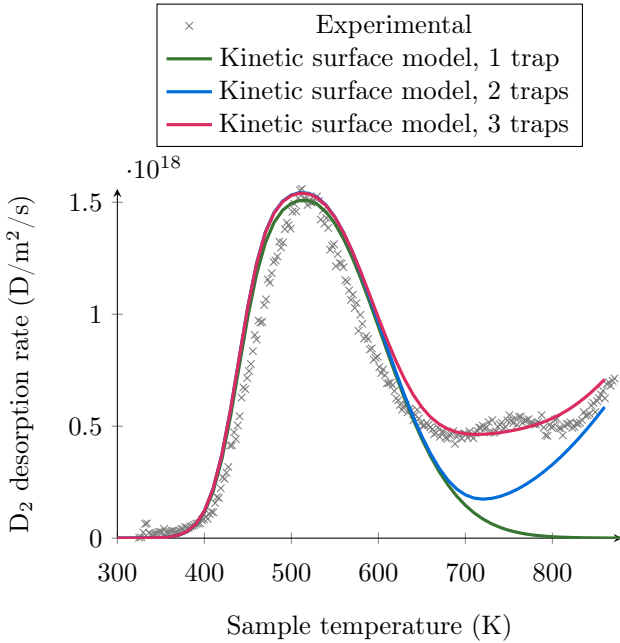


Figure 7: Experimental and simulated TDS spectra. Optimization is performed using Hypertomate solubility and the kinetic surface model. Fits obtained with one, two and three traps are displayed, showing that the trapping behaviour is best represented with three traps.

the fit in the 750 K region. For the sake of comparison, the result obtained with only one trap is also shown.

The parameters values obtained with the surface model fit are given in table 4.

## 4. Discussion

### 4.1. Permeation and TDS coupling

Permeation experiments have resulted in values for diffusivity  $D(T)$ , solubility  $K(T)$  and permeability  $\Phi(T)$

that have been shown to be in good agreement with permeation literature. These experiments also yielded trapping parameters corresponding to the dominant trapping site in Eurofer97, namely  $E_b$  and  $N_t$ :

$$E_b = 0.42 \text{ eV}$$

$$N_t = 6.08 \cdot 10^{25} \text{ m}^{-3}$$

As shown in figure 1, detrapping, binding and diffusion energies are linked by

$$E_{\text{dt}} = E_D + E_b$$

Using the values determined by permeation ( $E_D = 0.16 \text{ eV}$  and  $E_b = 0.42 \text{ eV}$ ), we obtain

$$E_{\text{dt, permeation}} = 0.58 \text{ eV}$$

This value is close to the detrapping energy corresponding to the main trapping site ( $E_{\text{dt},1} = 0.51 \text{ eV}$ ) visible on the TDS of Eurofer97. The trapping densities found with both experiments are also very close, showing that the two experiments are in agreement. Furthermore, we can see that  $N_{t,1} \gg N_{t,2}$  and  $N_{t,1} \gg N_{t,3}$ , which confirms the assumption made in equations (4) and (5) that trapping is dominated by one site in Eurofer97.

### 4.2. Recombination rate and solubility models

This part presents simulations performed with the recombination rate and solubility surface models. Traps energies and densities keep the values found in the previous part. In the solubility model, the boundary condition follows Sieverts' law with  $K$  taken from Hypertomate. In the recombination model, recombination rate  $K_r$  is evaluated using equation (13), meaning that the kinetic surface processes are assumed to be in steady-state. The

Name	Symbol	Value	Unit
Detrapping energies	$E_{dt,1}$	0.51	
	$E_{dt,2}$	1.27	eV
	$E_{dt,3}$	1.65	
Traps densities	$N_{t,1}$	$6.01 \cdot 10^{25}$	
	$N_{t,2}$	$6.44 \cdot 10^{22}$	$m^{-3}$
	$N_{t,3}$	$3.88 \cdot 10^{23}$	
Surface energies	$E_A$	1.32	
	$E_R$	0.65	eV
	$2E_{des}$	0.80	

Table 4: Detrapping energies, traps densities and surface energies  $E_A$ ,  $E_R$  and  $E_{des}$  resulting from the TDS fit with MHIMS and a kinetic surface model

values taken for  $E_A$ ,  $E_R$ ,  $E_{des}$  are those obtained in the kinetic surface model fit. The resulting values for  $K_r$  and  $K_d$  are given in table 5 and a visualization of the simulated TDS spectra corresponding to each of the three models is given in figure 8.

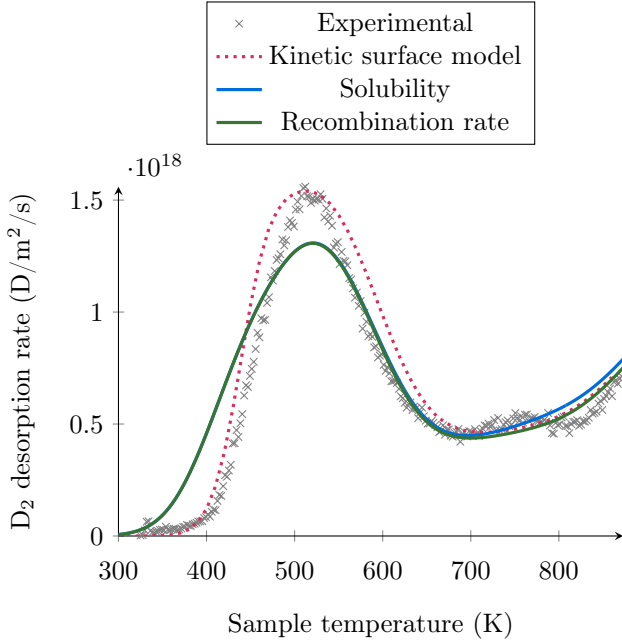


Figure 8: Experimental and simulated TDS spectra comparing the kinetic surface model, solubility and recombination rate boundary condition.

The kinetic surface model solution is shown with a dotted

Symbol	Unit	Kinetic model eqv.	Optimized
$K_{r0}$	$m^4 \cdot s^{-1}$	$7.35 \cdot 10^{-28}$	$1.99 \cdot 10^{-20}$
$E_{K_r}$	eV	-0.54	+0.73
$K_{d0}$	$mol^2 \cdot m^{-2} \cdot s^{-1} \cdot Pa^{-1}$	$2.28 \cdot 10^{-29}$	$2.23 \cdot 10^{26}$
$E_{K_d}$	eV	0	-1.27

Table 5: Recombination and dissociation rates used in the recombination rate simulations. Surface model equivalent is based on (13) and surface energies obtained from the fit, optimized ones come from the parametric optimization described in 4.2.

line for the sake of comparison. The solubility simulation shows a satisfying fit in the 600 K - 800 K region, but fails to replicate the initial desorption taking place in the 300 K - 500 K range. This higher initial desorption also lowers the main peak, as particles get desorbed at lower temperatures. Recombination and solubility solutions coincide in the 300 K - 900 K temperature range presented in figure 8, which was to be expected, as both models correspond to the steady-state of the surface model. In particular, this shows that steady-state of the kinetic surface model cannot be assumed to simulate properly this TDS experiment. Based on the activation energies used in the kinetic surface model, the limiting step for desorption is the bulk to surface transition, which energy barrier is 0.65 eV. This energy barrier inhibits the bulk to surface processes under 400 K: in this range, desorption is limited by the bulk to surface flux, i.e. the assumption that all processes are in steady-state does not apply. Thus, the solubility and steady-state recombination rate models cannot be used to describe the initial desorption profile seen in the experimental results.

However, if equation (13) is no longer taken into account,  $K_{r0}$  and  $E_{K_r}$  become free parameters that can be optimized in order to replicate the kinetic surface model with a recombination rate model. The spectra resulting from this optimization, performed using the optimization routine first introduced in [30], are presented in figure 9.

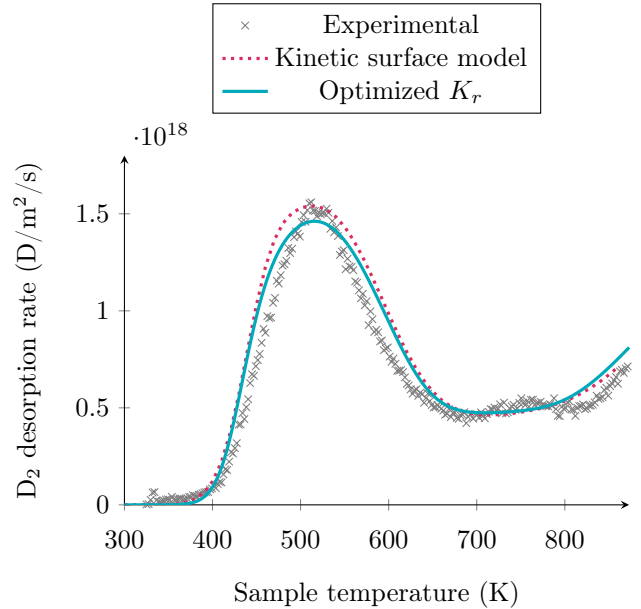


Figure 9: Experimental and simulated TDS spectra comparing the kinetic surface model with the optimized  $K_r$  model

This plot shows that the recombination rate can be used to replicate the experimental desorption flux in the 300 K - 500 K range. The optimized recombination energy is now positive (meaning that the recombination rate will increase with the temperature) and switches from -0.54 eV to 0.73 eV. Thus, the kinetic surface model and

the optimized recombination rate model both require the limiting step to have an activation energy of about 0.7 eV. However, the optimized recombination rate is just a fitting parameter with little physical meaning, while the kinetic surface model corresponds to a more careful description of the elementary processes taking place at the surface. Thus, the recombination rate needs to be handled with caution as discussed in [31].

## 5. Conclusion

Using the Hypertomate setup, the gas permeation technique has been used on Eurofer97 to determine its hydrogen diffusivity, solubility and permeability. The results were shown to be in good agreement with literature and showed that effective diffusivity and solubility are affected by traps in the investigated temperature range. In order to get a more detailed understanding of this trapping behaviour, TDS experiments on deuterium-loaded samples were performed to further investigate trapping in Eurofer97. The resulting spectrum presents several traps, similarly to [15]. In this work, the multiple-peak TDS spectrum was fitted using the MHIMS code including a kinetic surface model describing the elementary processes of hydrogen on Eurofer97 surface: dissociation, adsorption, desorption, absorption and (re-)surfacing. This parametric fit showed that three traps are necessary to model the trapping behaviour of deuterium in Eurofer97, which energies and densities were evaluated. The results of both experiments were shown to be in good agreement. In order to assess the improvement brought to the simulations by the kinetic surface model, fits with a recombination boundary condition were performed. As the initial value of  $K_r$  evaluated from the surface parameters failed to describe the initial desorption, a fit was performed with  $K_r$  left as a free parameter, showing that the recombination parameter can be tuned to fit the TDS, although the corresponding values differ widely from the initial ones and no longer describe the surface processes. A set of parameters describing adsorption and absorption of deuterium on the surface was also given, based on the TDS fit.

## Acknowledgments

This work has been carried out within the framework of the EUROfusion Consortium and has received funding from the Euratom research and training programme 2014-2018 and 2019-2020 under grant agreement no. 633053. The views and opinions expressed herein do not necessarily reflect those of the European Commission.

- [1] A. Kohyama, A. Hishinuma, D. S. Gelles, R. L. Klueh, W. Dietz, K. Ehrlich, Low-activation ferritic and martensitic steels for fusion application, *Journal of Nuclear Materials* 233-237 (1996) 138–147.
- [2] G. Federici, L. Boccaccini, F. Cismondi, M. Gasparotto, Y. Poitevin, I. Ricapito, An overview of the EU breeding blanket design strategy as an integral part of the DEMO design effort, *Fusion Engineering and Design* 141 (2019) 30–42.
- [3] E. A. Hodille, X. Bonnin, R. Bisson, T. Angot, C. S. Becquard, J. M. Layet, C. Grisolia, Macroscopic rate equation modeling of trapping/detrapping of hydrogen isotopes in tungsten materials, *Journal of Nuclear Materials* 467 (2015) 424–431.
- [4] E. Hodille, A. Založnik, S. Markelj, T. Schwarz-Selinger, C. Becquard, R. Bisson, C. Grisolia, Simulations of atomic deuterium exposure in self-damaged tungsten, *Nuclear Fusion* 57 (5) (2017) 056002.
- [5] G. Esteban, A. Peña, I. Urra, F. Legarda, B. Riccardi, Hydrogen transport and trapping in Eurofer97, *Journal of Nuclear Materials* 367-370 (2007) 473–477.
- [6] A. Aiello, I. Ricapito, G. Benamati, R. Valentini, Hydrogen isotopes permeability in Eurofer97 martensitic steel, *Fusion Science and Technology* 41 (2017) 872–876.
- [7] Z. Chen, X. Hu, M. Ye, B. D. Wirth, Deuterium transport and retention properties of representative fusion blanket structural materials, *Journal of Nuclear Materials* 549 (2021) 152904.
- [8] N. Baluc, D. Gelles, S. Jitsukawa, A. Kimura, R. Klueh, G. Odette, B. van der Schaaf, J. Yu, Status of reduced activation ferritic/martensitic steel development, *Journal of Nuclear Materials* 367-370 (2007) 33–41.
- [9] G. A. Esteban, L. A. Sedano, B. Mancinelli, K. Douglas, Diffusion and surface-limited transport parameters of deuterium in Incoloy 800, *Tech. rep.*, I-21020 Ispra - Italy (2001).
- [10] S. W. Rutherford, D. D. Do, Review of time lag permeation technique as a method for characterisation of porous media and membranes, *Adsorption* 3 (1997) 283–312.
- [11] C. S. Marchi, B. P. Someday, S. Robinson, Permeability, solubility and diffusivity of hydrogen isotopes in stainless steels at high gas pressures, *International Journal of Hydrogen Energy* 32 (2006) 100–116.
- [12] E. Malitckii, Y. Yagodzinskyy, M. Ganchenkova, S. Binyukova, H. Hänninen, R. Lindau, P. Vladimirov, A. Moeslang, Comparative study of hydrogen uptake and diffusion in ODS steels, *Fusion Engineering and Design* 88 (9) (2013) 2607–2610.
- [13] Y. Yagodzinskyy, E. Malitckii, M. Ganchenkova, S. Binyukova, O. Emelyanova, T. Saukkonen, H. Hänninen, R. Lindau, P. Vladimirov, A. Moeslang, Hydrogen effects on tensile properties of Eurofer 97 and ODS-Eurofer steels, *Journal of Nuclear Materials* 444 (1) (2014) 435–440.
- [14] Y. Xu, Z.-S. Wu, L.-M. Luo, X. Zan, X.-Y. Zhu, Q. Xu, Y.-C. Wu, Transport parameters and permeation behavior of hydrogen isotopes in the first wall materials of future fusion reactors, *Fusion Engineering and Design* 155 (2020) 111563.
- [15] Y. Martynova, M. Freisinger, A. Kreter, B. Göths, S. Möller, A. Terra, D. Matveev, M. Rasiński, B. Unterberg, S. Brezinsek, C. Linsmeier, Impact of Kr and Ar seeding on D retention in ferritic-martensitic steels after high-fluence plasma exposure, *Nuclear Materials and Energy* 17 (2018) 307–313.
- [16] O. Ogorodnikova, Z. Zhou, K. Sugiyama, M. Balden, Y. Gasparyan, V. Efimov, Surface modification and deuterium retention in reduced-activation steels under low-energy deuterium plasma exposure. part I: undamaged steels, *Nuclear Fusion* 57 (3) (2016) 036010.
- [17] M.-F. Maday, L. Pilloni, Hydrogen effects on the tensile and fatigue properties of Eurofer97, *Fusion Engineering and Design* 75-79 (2005) 957–961.
- [18] A. Hollingsworth, M. Y. Lavrentiev, R. Watkins, A. Davies, S. Davies, R. Smith, D. Mason, A. Baron-Wiechec, Z. Kollo, J. Hess, I. Jepu, J. Likonen, K. Heinola, K. Mizohata, E. Meslin, M.-F. Barthe, A. Widdowson, I. Grech, K. Abraham, E. Pender, A. McShee, Y. Martynova, M. Freisinger, A. D. Backer, Comparative study of deuterium retention in irradiated Eurofer

- and Fe–Cr from a new ion implantation materials facility, *Nuclear Fusion* 60 (2020) 016–024.
- [19] E. A. Hodille, L. Begrambekov, J. Pascal, O. Saidi, J. M. Layet, B. Pégourié, C. Grisolia, Hydrogen trapping in carbon film: From laboratories studies to tokamak applications, *International Journal of Hydrogen Energy* 39 (2014) 20054–20061.
- [20] V. Oliveira, K. Zilnyk, H. Sandim, Thermodynamic simulation of reduced activation ferritic-martensitic Eurofer97 steel, *Journal of Phase Equilibria and Diffusion* 38 (2017) 208–216.
- [21] A. McNabb, P. K. Foster, A new analysis of the diffusion of hydrogen in iron and ferritic steels, *Transactions of the Metallurgical Society of AIME* 27 (1963) 227–618.
- [22] K. Schmid, V. Rieger, A. Manhard, Comparison of hydrogen retention in W and W/Ta alloys, *Journal of Nuclear Materials* 426 (2012) 247–253.
- [23] G. R. Longhurst, TMAP7 user manual, Tech. rep. (2008).
- [24] R. Delaporte-Mathurin, E. A. Hodille, J. Mougenot, Y. Charles, C. Grisolia, Finite element analysis of hydrogen retention in ITER plasma-facing components using FESTIM, *Nuclear Materials and Energy* 21 (2019) 100709.
- [25] F. Sun, X. Li, L. Zhang, M. Nakata, M. Zhao, T. Wada, S. Yamazaki, A. Koike, Y. Oya, Modeling and simulation for surface helium effect on hydrogen isotopes diffusion and trapping/detrapping behavior in plasma facing materials, *Journal of Nuclear Materials* 537 (2020) 152227.
- [26] F. Waelbroeck, P. Wienhold, J. Winter, E. Rota, T. Banno, Influence of bulk and surface phenomena on the hydrogen release out of clean metallic surfaces, KFA report JUL-1966 Forschungszentrum Jülich.
- [27] M. Pick, K. Sonnenberg, A model for atomic hydrogen metal interactions - application to recycling, recombination and permeation, *Journal of Nuclear Materials* 131 (2) (1985) 208–220.
- [28] A. Boda, S. M. Ali, K. T. Shenoy, S. Mohan, Adsorption, Absorption, Diffusion, and Permeation of Hydrogen and Its Isotopes in bcc Bulk Fe and Fe(100) Surface: Plane Wave-Based Density Functional Theoretical Investigations, *The Journal of Physical Chemistry C* 123 (39) (2019) 23951–23966.
- [29] W. P. Davey, Precision measurements of the lattice constants of twelve common metals, *Phys. Rev.* 25 (1925) 753–761.
- [30] R. Delaporte-Mathurin, E. A. Hodille, J. Mougenot, Y. Charles, C. Grisolia, Parametric optimisation based on TPD experiments for rapid and efficient identification of hydrogen transport materials properties, submitted to *Nuclear Materials and Energy*.
- [31] K. Schmid, M. Zibrov, On the use of recombination rate coefficients in hydrogen transport calculations, *Nuclear Fusion* 61 (8) (2021) 086008.